



Lowest threshold lasing modes localized on marginally unstable periodic orbits in a semiconductor microcavity laser

IN-GOO LEE,¹ CHANG-HWAN YI,¹ JI-WON LEE,² HYEON-HYE YU,¹
JINHYEOK RYU,¹ SUNJAE GWAK,¹ HYUNDONG KIM,¹
KWANG-RYONG OH,³ AND CHIL-MIN KIM^{1,*}

¹Department of Emerging Materials Science, DGIST, Daegu 42988, South Korea

²Optics & Mechatronics Equipment Group, Samsung Electro-Mechanics, Suwon 16674, South Korea

³IT Convergence and Components Lab. ETRI, Daejeon 34129, South Korea

*chmkim@dgist.ac.kr

Abstract: The lowest threshold lasing mode in a rounded D-shape microcavity is theoretically analyzed and experimentally demonstrated. To identify the lowest threshold lasing mode, we investigate threshold conditions of different periodic orbits by considering the linear gain condition due to the effective pumping region and total loss consisting of internal and scattering losses in ray dynamics. We compare the ray dynamical result with resonance mode analysis, including gain and loss. We find that the resonance modes localized on the pentagonal marginally unstable periodic orbit have the lowest threshold in our fabrication configuration. Our findings are verified by obtaining the path lengths and far-field patterns of lasing modes.

© 2020 Optical Society of America under the terms of the [OSA Open Access Publishing Agreement](#)

1. Introduction

Microcavity lasers have attracted much attention owing to the high-quality factor of their whispering gallery modes, which are supported by total internal reflection. A circular microcavity has been spotlighted because of its extremely high-quality factor [1] and the potential for highly sensitive label-free detection [2–5] and gyroscopy [6,7]. Currently, it has been reported that deformed microcavities from the circular one have various outstanding characteristics such as directionality [8–16] and chirality [13,17] with minimized degradation of high-quality factor, which are crucial for wide-range applications.

When a deformed semiconductor microcavity laser is excited by current injection, it is hard to excite a whole cavity region because the area of the contact region for pumping is smaller than the cavity surface due to fabricating limitation. Because of this reason, periodic orbits in a deformed microcavity are partially overlapped with the contact region. Accordingly, the modes localized on them are excited only along the overlapped parts of the periodic orbits near the threshold (i.e., we rule out the current diffusion at higher current injection). This “partial excitation” makes different threshold conditions for lasing of resonance modes localized on the periodic orbits. In other words, the lasing modes are conditionally determined by pumping circumstances: the lasing threshold of a certain resonance mode is strongly dependent on its loss and the effective pumping rate [18]. The smaller contact region compared to the cavity for injection current is very natural and general in fabricating two-dimensional semiconductor lasers. However, a lasing threshold condition connecting the loss and partial excitation of periodic orbits in a microcavity laser has not been well analyzed so far. Hence, in the present paper, we aim to study their relations explicitly.

To study the lowest threshold lasing mode, we take a semiconductor microcavity defined by a rounded D-shape (RDS) boundary morphology. In this shape of the microcavity, there exist unstable periodic orbits (UPOs) and marginally unstable periodic orbits (MUPOs). Here,

MUPOs exhibit segmented-continuous curve structures originating from the invariant curves of non-isolated periodic orbits in phase space of a circular cavity. While, the modes localized on MUPOs slowly decay to leaky regions owing to the stickiness of classical rays in the vicinity of them [19,20], the ones on UPOs decay quickly. This implies that, modes localized on MUPOs are advantageous for lasing over those localized on UPOs, known as scarred modes [21]. Through numerical and experimental analyses, we investigate lasing threshold conditions of resonance modes localized on UPOs and MUPOs. In numerical investigations, we make a prediction for the lowest threshold lasing modes, which is deduced in terms of the effective pumping region (i.e., partial excitation) in both ray dynamics and resonance mode analysis. To obtain the threshold condition in ray dynamics, we calculate the gain due to the effective pumping region and the total loss consisting of internal and scattering losses. Also, in the resonance mode analysis, the threshold pumping strength is obtained by using the spatial wave function and complex wavenumber of resonance modes. This numerical prediction is clearly confirmed in the experiments.

2. Rounded D-shape microcavity laser

An RDS microcavity comprises three circular arcs and one linear section, as shown in Fig. 1(a). The main circular arc with a radius of $R = 30 \mu\text{m}$ is tangentially connected to two smaller circular arcs with a radius of $r = 0.5R$ at an angle ϕ from the y-axis. The linear section is tangentially connected to the two smaller arcs. We set the angle $\phi = 80^\circ$, where the cavity has various MUPOs and UPOs. Our system is fabricated based on seven-layered multi-quantum-well (MQW) surrounded by InGaAsP separate-confinement-heterostructure (SCH). This core structure is interposed between the n-doped InP substrate at the bottom layer with a buffer zone and by a p-doped InP cladding layer at the top layer. Finally, a p-doped InGaAs ohmic layer is grown at the uppermost surface. The whole structure is illustrated in Fig. 1(b). The active layer consists seven

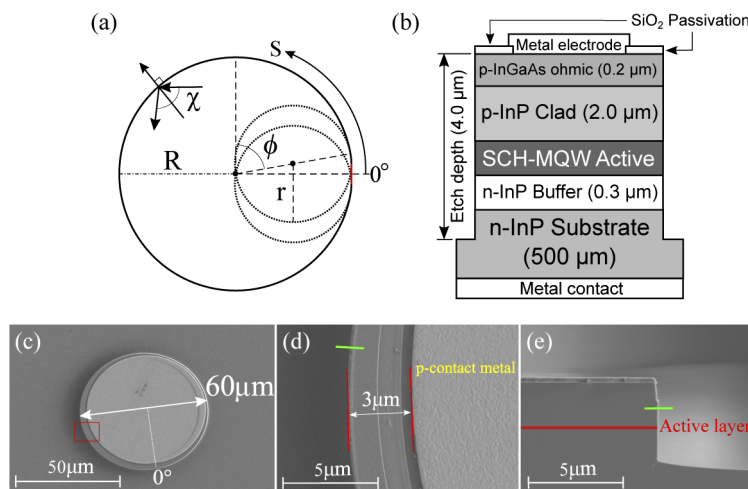


Fig. 1. An RDS semiconductor microcavity laser. (a) is a schematic of our RDS microcavity with $\phi = 80^\circ$ and $r = 0.5R$. A linear section between the smaller arcs is highlighted by red color. (b) shows a stack layer diagram of an InP-based semiconductor laser along the vertical cross-section. (c) is an SEM image of a fabricated RDS microcavity laser. (d) is a zoomed image of the red square region in (c) showing the $3 \mu\text{m}$ inward gap between the contact region and the sidewall. (e) shows a vertical cross-section of RDS embedding an SCH-MQW active layer marked by a red band. Green bars in (d) and (e) represent the length of λ .

pairs of a 0.8% compressively strained InGaAsP well ($\lambda_g = 1.68 \mu\text{m}$, 72 thick) and a 0.60% tensile strained InGaAsP barrier ($\lambda_g = 1.31 \mu\text{m}$, 105 thick), and undoped InGaAsP separate confinement layers (see Ref. [22,23] for details). The laser was etched $4 \mu\text{m}$ deep into an RDS cross-section by inductively coupled plasma etching. The SiO_2 passivation layer is deposited by using the PECVD to define the current contact region where the electrode and ohmic layer adjoin. The boundary of this contact region was defined along the sidewall of the microcavity with a $3 \mu\text{m}$ inward gap. A p-contact Ti/Au metal electrode was deposited through the lift-off process [24] to set the current contact layer. The scanning electron microscope (SEM) image of the full structure of our laser is shown in Fig. 1(c); Fig. 1(d) shows the $3 \mu\text{m}$ gap between the sidewall and electrode. Although the electrode was slightly misaligned, this misalignment does not affect the experimental results because the electrode is large enough to cover the entire contact region.

3. UPOs and MUPOs in the RDS cavity

The phase space $(q, p) \equiv (S/S_{\text{max}}, p_0 \sin \chi)$ of our cavity is constructed by the canonical conjugate variables S and p : S is the boundary length from the point $\theta = 0^\circ$, S_{max} the total boundary length, and p the tangential momentum of the ray for the incident angle χ at S with the initial momentum of $p_0 \equiv 1$. Because there is no recognizable stable periodic orbits, the overall structure of phase space follows a fully chaotic property. To reveal MUPOs and UPOs, we numerically obtain the chaotic repeller distribution (CRD) [25] and survival probability distribution (SPD) [19,20,26], as shown in Fig. 2 through ray dynamical simulations. For calculations of CRD, we follow the schemes used in Ref. [25]. MUPOs and UPOs above the critical line are observed and highlighted by red-straight curves and green squares, respectively. MUPOs and UPOs in Fig. 2(a) are labeled by the number of rotations (r) and reflections (t) as follows: $p_{r,t} = p_{1,3}, p_{1,4}, p_{1,5}, p_{1,6}$ MUPOs and $p_{1,4}, p_{1,5}$ UPOs.

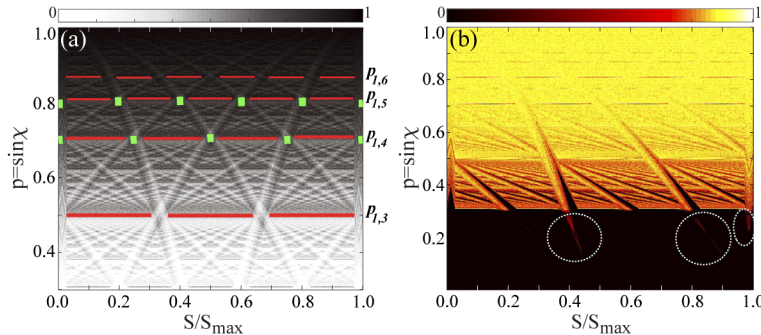


Fig. 2. Ray dynamical simulation of the RDS cavity. (a) is CRD, which shows chaotic saddles possessing marginally unstable periodic orbits (red) and unstable periodic orbits (green). (b) is normalized SPD in a logarithmic scale. Three dotted circles around $S/S_{\text{max}} = 0.4, 0.8, \text{ and } 1.0$ indicate emission windows.

The emission properties of the RDS cavity are investigated by means of the survival probability distributions for TE polarized rays applying the Fresnel equations [19,20,26]. SPD in a logarithmic scale in Fig. 2(b) elucidates the emission windows below the critical line through the unstable manifolds of chaotic saddles [19,20,27–29]. The figure shows three emission windows marked by dotted circles around $S/S_{\text{max}} = 0.4, 0.8, \text{ and } 1.0$ for the counter-clockwise (CCW) traveling rays ($p > 0$). Due to the mirror-reflection symmetry of RDS, three emission windows for clockwise (CW) traveling rays are located at $S/S_{\text{max}} = 0.0, 0.2, \text{ and } 0.6$.

To estimate the scattering loss of each periodic orbit, it is useful to implement the survival probability time distribution (SPTD) [30] of ray dynamical simulation. Because the scattering

loss is usually expressed in decibels per centimeter (dB/cm), our SPTD at time $t = l/c$, where c is the speed of light, is obtained as an averaged survival intensity normalized by an initial intensity of I_0 in decibel unit as follows :

$$\langle L_I \rangle_l \equiv 10 \log \langle I_N/I_0 \rangle_l = 10 \log \left(\frac{1}{N} \sum_n r_n \right)_l \approx -\alpha_s l, \quad (1)$$

where I is the survival intensity given by the reflection probability r at the propagating time l , N is the number of rays taken into account for our computation, and α_s is the decaying ratio giving rise to the scattering loss

$$\alpha_s = -\frac{d\langle L_I \rangle}{dl}. \quad (2)$$

Figure 3 shows SPTDs computed by $N = 100$ initial rays of $I_0 = 1$ starting from the vicinity of periodic orbits. In the figure, the linear fitting curves of SPTDs deduce the scattering loss α_s . It is important to note that even a small roughness of cavity boundaries can affect the lasing of modes [31]. However, as is shown in Figs. 1(d) and (e), the surface roughness of our microcavity is much tiny compared to the wavelength emitted from our microcavity so that we can rule out the scattering loss factor provoked by the surface roughness in our modeling.

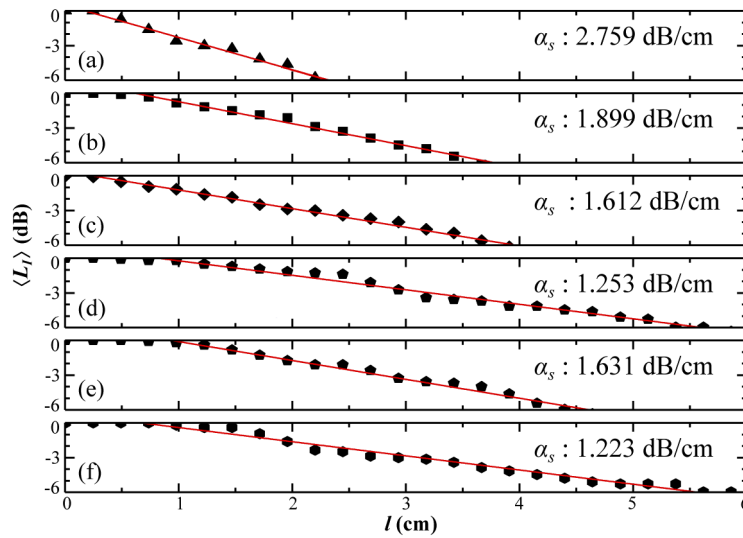


Fig. 3. Semi-logarithmic plots of survival probability time distributions (discrete symbols) and their linear fittings (straight curves) for each periodic orbit. (a) $p_{1,3}$ MUPO, (b) $p_{1,4}$ MUPO, (c) $p_{1,4}$ UPO, (d) $p_{1,5}$ MUPO, (e) $p_{1,5}$ UPO, and (f) $p_{1,6}$ MUPO. From the slopes of the fitting curves, the decaying exponent α_s with respect to the effective propagation time of the propagation length with a constant velocity of rays is obtained.

Resonance modes in our RDS cavity are obtained by using the boundary element method [32] in the region $n_e k R \sim 396$, which matches the experimental one. Here, n_e , k , and R denote the effective refractive index of 3.3, the vacuum wavenumber, and the radius of the main circle in Fig. 1(a), respectively. Wavenumbers of resonance mode groups localized on MUPOs and UPOs are shown in Fig. 4(a). The regular interval $\text{Re}(\Delta k R)$ of each mode group identified in Fig. 4 corresponds to a periodic orbit in the sense of the relation $L_p^{\text{res}}/R = 2\pi/n_e \Delta k R$, where L_p^{res} is the periodic orbit length. The average intervals $\langle \Delta k R \rangle$ of the resonance mode groups and corresponding path lengths are shown in Table 1 for $R = 30 \mu\text{m}$. This result agrees well

with the classical path lengths L_p^{ray} obtained by ray dynamical calculations, i.e., geometries of periodic orbits. By exemplifying representative highest-Q modes, which are marked by dotted-red squares in Fig. 4(a), it is confirmed that spatial wave patterns and their Husimi distributions are well-matched with the periodic orbits inferred, as are shown in Fig. 4(b) [32,33].

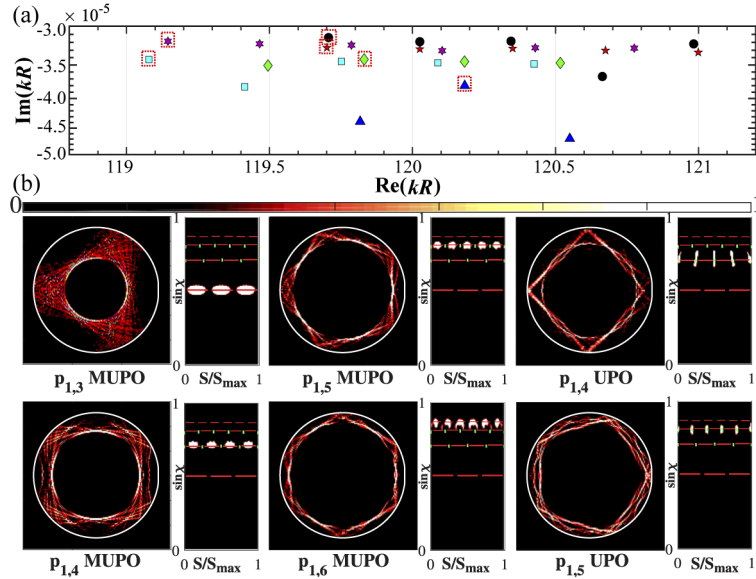


Fig. 4. Passive resonance modes for the RDS cavity. (a) is the eigenvalue distribution of $p_{1,3}$ (blue triangle), $p_{1,4}$ (cyan square), $p_{1,5}$ (red pentagram), and $p_{1,6}$ MUPO (black circle) and $p_{1,4}$ (green diamond) and $p_{1,5}$ UPO (purple hexagram) in the region $n_e kR \sim 396$. The eigenvalues of representative modes marked with dotted-red boxes are $120.2018 - i3.8006 \times 10^{-5}$ for $p_{1,3}$ MUPO, $119.0782 - i3.4248 \times 10^{-5}$ for $p_{1,4}$ MUPO, $119.7007 - i3.2675 \times 10^{-5}$ for $p_{1,5}$ MUPO, $119.7075 - i3.1429 \times 10^{-5}$ for $p_{1,6}$ MUPO, $119.8308 - i3.4238 \times 10^{-5}$ for $p_{1,4}$ UPO, and $119.1448 - i3.1848 \times 10^{-5}$ for $p_{1,5}$ UPO. (b) is the spatial wave patterns and their Husimi distributions of representative modes. We overlap the Husimi distribution on the periodic orbits in CRD to make clear the mode localization.

Table 1. Path lengths of periodic orbits for our RDS microcavity

Periodic orbit		$\langle \Delta kR \rangle$	$L_p^{\text{res}} (\mu\text{m})$	$L_p^{\text{ray}} (\mu\text{m})$
MUPO	$p_{1,3}$	0.3665	155.85	155.88
	$p_{1,4}$	0.3352	170.41	169.71
	$p_{1,5}$	0.3246	175.97	176.34
	$p_{1,6}$	0.3195	178.78	180.00
UPO	$p_{1,4}$	0.3362	169.90	169.50
	$p_{1,5}$	0.3293	173.46	175.82

4. Linear gain condition at the threshold

Now, we discuss the robustness of the lasing of resonance modes supported by MUPOs and UPOs in terms of the lowest threshold conditions. The general lasing condition for a semiconductor

laser is expressed by the following inequality:

$$G > \alpha_i + \alpha_s = \alpha_i + \frac{1}{L_p} \log \frac{1}{R}, \quad (3)$$

where G is the gain, α_i the internal loss, α_s the scattering loss, L_p the orbit path length of a mode, and R the survival ratio per cycle. This inequality simply implies that when the gain of certain modes in the active medium is greater than the total loss of the modes, the mode can lase above the threshold, i.e., $G = \alpha_i + \alpha_s$. From now on, we will use the single-mode approximation and disregard modal interactions to simplify our problems in analyzing a lasing mode at the lowest threshold condition of the RDS microcavity laser [18,34]. Note that, strictly speaking, the full version of the Maxwell–Bloch equations should be solved numerically taking nonlinear modal interactions [34,35] into account to investigate the general lasing modes.

Because an inward gap exists between the contact region and the sidewall of our microcavity laser, the effective pumping region is limited by the contact region, and only partial trajectories of periodic orbits are overlapped with this effective pumping region. To reflect this partial pumping condition in our derivations, we define an effective excited length L_e , then the gain in the threshold condition can be modified as follows:

$$G'_{\text{th}} = \frac{L_e}{L_p} \times G_{\text{th}} = \Gamma g \frac{L_e}{L_p} (J_{\text{th}} - J_0) = \alpha_i + \alpha_s, \quad (4)$$

where L_e is the excited length, L_p the path length, G_{th} the gain at the threshold, Γ the confinement factor, g the gain coefficient, J_{th} the threshold current density, and J_0 the transparency current density. The transparency current and the internal loss can be assumed to be constant for the same sample, because they depend solely on material compositions of InGaAsP SCH-MQW gain layer. In other words, the scattering loss is the only functional factor to determine the threshold current density for each periodic orbit. Under this assumption, the threshold current density can be expressed as follows [36,37]:

$$J_{\text{th}} = J_0 + \frac{L_p/L_e}{\Gamma g} (\alpha_i + \alpha_s) = J_0 + C_1 p_c, \quad (5)$$

where $C_1 \equiv 1/\Gamma g$ is a constant and $p_c \equiv (\alpha_i + \alpha_s)L_p/L_e$ is the threshold parameter. Note that the parameter p_c depends both on the trajectories of the periodic orbits and the effective pumping region.

As are shown in Fig. 4(b), wave functions $\psi(x, y)$ of resonance modes are broadly distributed, though they are localized mainly along the classical periodic orbits. Hence, based on the schemes used in Ref. [18], we can derive the threshold condition of lasing modes by further assuming that the real part of a wavenumber (frequency) of a mode is almost the same as the center of the gain spectrum (or the gain spectrum is broad enough to cover the resonance modes that we obtained) [18,34]. Subsequently, the threshold pumping strength W_{th} is expressed by:

$$W_{\text{th}} = \frac{n_e^2 \gamma}{2\pi \rho \kappa^2 \hbar} \frac{-\text{Im}(k) + \beta}{\text{Re}(k)} \frac{\int_D dx dy |\psi(x, y)|^2}{\int_D dx dy |\psi(x, y)|^2 \Theta(x, y)} = C_2 p_w, \quad (6)$$

where ρ is the carrier density, κ the coupling strength, γ the relaxation rate for TE polarized light, k the resonant wavenumber for a passive cavity, β the background absorption, D the cavity region, ψ the spatial wave function, and Θ the pumping characteristic function, which takes "1" inside the effective pumping region and "0" otherwise. Here, β can be expressed by the internal loss α_i as $\beta = \eta \alpha_i / 2n_e$, where η is the scale factor of 3×10^{-5} in this case. The above equation can be simplified by reducing the constant as $C_2 \equiv n_e^2 \gamma / 2\pi \rho \kappa^2 \hbar$ and by defining the threshold parameter as $p_w \equiv [(-\text{Im}(k) + \eta \alpha_i / 2n_e) \int_D dx dy |\psi(x, y)|^2] / [\text{Re}(k) \int_D dx dy |\psi(x, y)|^2 \Theta(x, y)]$.

Obviously, the main factor to determine the threshold pumping strength W_{th} is the threshold parameter p_w , which depends on the fraction of wave functions overlapped with the effective pumping region. This effective pumping region is controlled by adjusting the profiles of the function $\Theta(x, y)$ in Eq. (6) for theoretical prediction. Figure 5 shows the parameters p_c in Eq. (5) and p_w in Eq. (6) as a function of the “effective inward gap” $\equiv l_g$: distance between the effective pumping region and the sidewall. In obtaining p_c and p_w in Fig. 5, we exemplify the case of $\alpha_i = 6.8 \text{ cm}^{-1}$, which is reported in Ref. [38] for the eight-quantum-well structures. The mode, which has the lowest threshold parameter, can be the first-appearing lasing mode for each l_g . In the range $0.7 \mu\text{m} < l_g < 1.8 \mu\text{m}$, both parameters of p_c and p_w for $p_{1,5}$ MUPO exhibit the lowest values compared with the ones of other periodic orbits.

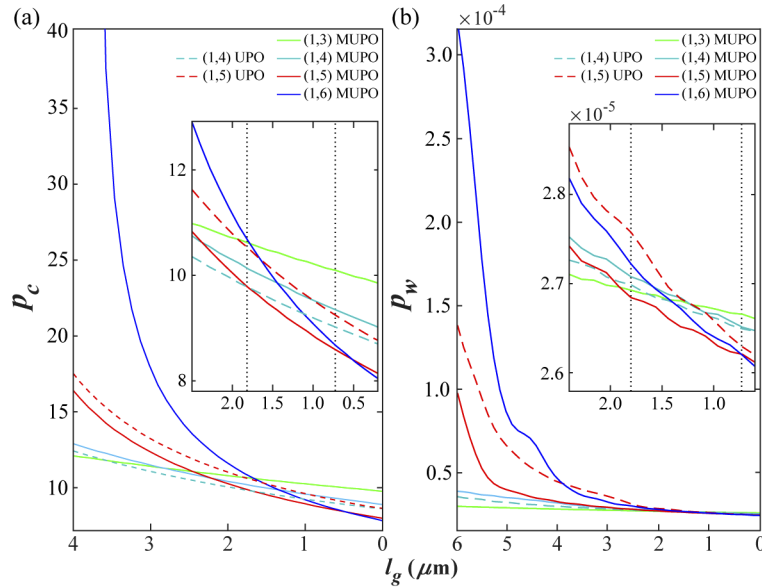


Fig. 5. Threshold parameters depending on the length of the inward gap between the sidewall and the effective pumping region at the gain layer. (a) and (b) are threshold parameters of p_c and p_w , respectively, which are defined by the classical excited length and the ratio of the sum of wave function inside the cavity and the sum of the overlapped wave function. Both results show a range of $0.7 \mu\text{m} < l_g < 1.8 \mu\text{m}$ for the lowest threshold parameter of $p_{1,5}$ MUPO. The insets are the magnified graphs, which show the lowest threshold parameters of $p_{1,5}$ MUPO.

Now, we compute the true effective pumping region and, in turn, the effective inward gap l_g taking into account the realistic parameters, which are used in our experiments. The effective pumping region inside the cavity is well defined, considering Ohm’s law ($\mathbf{J} = q\rho\mu\mathbf{E}$) and the continuity equation for drift current. In the procedures, the effects of small amount of direct diffusion current is neglected. Further assuming that the electric field inside a semiconductor drift region decreases linearly as the depth increases from the top electrode to the bottom ground, and that the effective pumping region has a discrete profile instead of a Gaussian profile, the effective pumping region A_{eff} is expressed by [39–41]

$$A_{\text{eff}} = \frac{I_0}{q\rho\mu(E_t - E_b)(1 - x/d) + E_b} = \frac{A_c}{1 + (A_c/A_e - 1)(1 - x/d)}, \quad (7)$$

where I_0 is the injection current, q the charge of an electron, μ the mobility of the semiconductor, E_t the electric field at the top electrode, E_b the electric field at the bottom of the cavity, x the

depth from the top electrode, d the height of the microcavity, A_c the area of the cavity, and A_e the area of the contact region. Because the active layer, i.e., the multi-quantum wells, of fabricated cavities [see Fig. 1(b)] was placed at a depth of $2.2 \mu\text{m}$ from the top, the effective inward gap l_g between the effective pumping region and the sidewall is obtained as $1.77 \mu\text{m}$ although the physical inward gap between the contact region and the sidewall is $3 \mu\text{m}$ for our RDS microcavity laser with $R = 30 \mu\text{m}$. The effective pumping region coincides well with the result of the threshold condition. This result implies that indeed the lasing modes localized on $p_{1,5}$ MUPO firstly appear at the lowest threshold injection current compared with the others in our experimental condition.

5. Experimental results and emission characteristics

We experimentally investigate the first lasing mode to verify our theoretical prediction. Our RDS laser is uniformly pumped through the electrode with continuous-wave injection current at the temperature of 20°C . In order to take the maximized laser output, we align a single-mode lensed fiber at $\theta = 150^\circ$, which is the predetermined direction fixed by preliminary experiments. The laser output is collected $10 \mu\text{m}$ away from the sidewall for the measurement of output power and emission spectra. Then, the collected laser output is split with a 50:50 optical coupler and equally distributed to an optical power meter and an optical spectrum analyzer. A far-field pattern (FFP) is measured $470 \mu\text{m}$ away from the sidewall.

Figure 6(a) shows the total output power and major peak intensity versus injection current. From the total output power (red) in Fig. 6(a), we can identify the lasing threshold near 44 mA . To see the threshold of the first lasing mode, the peak intensity of the first main lasing mode is measured as a function of the injection current (blue), and it is revealed that the threshold of this mode is almost the same as the one of the total output power as 44 mA . Because the sum of the internal and scattering losses is inversely proportional to the quality factor ($= Q$) of modes [37,42], we estimate it to obtain the total loss at the lasing threshold. By measuring a center wavelength, $\lambda_c \sim 1551 \text{ nm}$, of the major peak and its full width at half maximum, $w = 0.077 \text{ nm}$, [see Fig. 6(b)], it is obtained that $Q = \lambda_c/w \approx 2.0 \times 10^4$. Now, the internal loss α_i can be extracted by subtracting the scattering losses of $p_{1,5}$ MUPO, $\alpha_s = 1.253 \text{ cm}^{-1}$ [see Fig. 3(d)], from the total loss deduced from the experimental quality factor [37,42], as follows

$$\alpha_i + \alpha_s = \frac{2\pi n_e}{\lambda Q} \approx 7.36 \text{ cm}^{-1} \rightarrow \alpha_i \sim 6.1 \text{ cm}^{-1}. \quad (8)$$

This value of the internal loss is consistent with the previous results of semiconductor lasers [38,43,44] as well as the one used in Fig. 5.

Figure 6(c) shows the spectrum at the threshold current, where the prominent lasing peak is not noticeable. Above the threshold, a main lasing mode group (Group 1) is observed at 47 mA , as shown in Fig. 6(d), which lases at $\{1547.40, 1551.14, 1555.93 \text{ nm}\}$. Also, we can find another mode group (Group 2) at $\{1547.90, 1551.57, 1555.47 \text{ nm}\}$. The path length of each mode group can be calculated using the relation between the path length and the free spectral range as follows:

$$L_p = \frac{1}{N-1} \sum_{i=1}^{N-1} \frac{[(\lambda_i + \lambda_{i+1})/2]^2}{n_g \Delta\lambda}, \quad (9)$$

where N is the number of peaks in the mode group, n_g the group refractive index of 3.68 [45], λ_i the wavelength of the i -th peak in the mode group, and $\Delta\lambda$ the free spectral range. The resulting path lengths are $173.66 \mu\text{m}$ for the first lasing mode group and $172.99 \mu\text{m}$ for the other mode group; these values agree well with the path length of $p_{1,5}$ MUPO and $p_{1,5}$ UPO, respectively, with an accuracy above 98% .

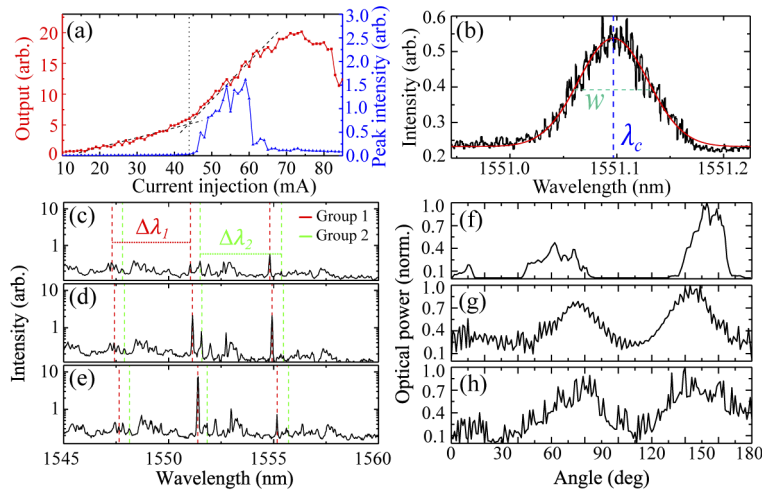


Fig. 6. Experimental results of the RDS semiconductor microcavity laser. (a) shows the total output power (red) and major peak intensity (blue) as functions of injection current. A vertical dotted line shows a threshold of lasing at 44 mA. (b) shows the line width w of the major peak $\lambda = \lambda_c$ (black) fitted by Gaussian curve (red) at the threshold current. The spectra in (c), (d), and (e) are measured at 44 mA, 47 mA, and 51 mA, respectively. Two mode groups in the spectra are marked by dashed-red lines (Group 1) and dashed-green lines (Group 2). (f) is the far-field pattern from the ray dynamical simulation, (g) is the average far-field pattern from the resonance modes localized on $p_{1,5}$ MUPO, and (h) is the far-field pattern from the experiments. All of the far-field patterns indicate three emission directions around $\theta = 10^\circ$, 70° , and 150° .

As a final remark, FFPs of the RDS microcavity laser obtained experimentally and numerically are compared. Figures 6(f)-(h) show FFPs of the ray dynamical simulation, the resonance modes localized on $p_{1,5}$ MUPO, and the experiments, respectively. All FFPs clearly reveal three emission directions toward $\sim 150^\circ$, $\sim 70^\circ$, and $\sim 10^\circ$ with the strongest emission at $\theta = 150^\circ$. These emission directions originate from the emission windows of $S/S_{\max} = 0.6$ (CW), 1.0 (CCW), and 0.2 (CW), respectively. Although the emission directions of the FFPs from the ray and wave simulation are slightly different, the nice overall agreement among the three FFPs indicates that the first lasing mode in our RDS microcavity laser is the mode localized on $p_{1,5}$ MUPO.

6. Conclusion

We have studied a rounded D-shape semiconductor microcavity laser excited by the continuous-wave injection current. Based on the fundamental linear gain condition with a single-mode lasing approximation, we predict that the modes localized on the pentagonal-shaped marginally unstable periodic orbit has the lowest threshold for lasing in our rounded D-shape microcavity laser, which has a $3 \mu\text{m}$ inward gap between the contact region and the sidewall. This prediction of the lowest threshold condition for lasing has been transparently verified in experiments. The path length deduced from ray dynamics, resonance modes, and experiments agreed well with the length of the pentagonal-shaped unstable and marginally unstable periodic orbits. Nice agreement of emission directions toward $\theta \sim 150^\circ$, $\sim 70^\circ$, and $\sim 10^\circ$ is obtained for all results of ray dynamics, resonance modes, and experiments. The results of the present work clearly reveal the fact that the lasing thresholds of the resonance modes are decisively affected by the effective pumping region and cavity morphology. In the same context, the lasing of scars reported in our previous study [46] can be explained without contradictions.

Funding

Ministry of Health and Welfare (HG18C0069).

Disclosures

The authors declare no conflicts of interest.

References

1. D. K. Armani, T. J. Kippenberg, S. M. Spillane, and K. J. Vahala, "Ultra-high-Q toroid microcavity on a chip," *Nature* **421**(6926), 925–928 (2003).
2. A. M. Armani, R. P. Kulkarni, S. E. Fraser, R. C. Flagan, and K. J. Vahala, "Label-free, single-molecule detection with optical microcavities," *Science* **317**(5839), 783–787 (2007).
3. F. Vollmer and S. Arnold, "Whispering-gallery-mode biosensing: label-free detection down to single molecules," *Nat. Methods* **5**(7), 591–596 (2008).
4. T. Lu, H. Lee, T. Chen, S. Herchak, J.-H. Kim, S. E. Fraser, R. C. Flagan, and K. Vahala, "High sensitivity nanoparticle detection using optical microcavities," *Proc. Natl. Acad. Sci.* **108**(15), 5976–5979 (2011).
5. L. He, Ş. K. Özdemir, J. Zhu, W. Kim, and L. Yang, "Detecting single viruses and nanoparticles using whispering gallery microlasers," *Nat. Nanotechnol.* **6**(7), 428–432 (2011).
6. S. Sunada and T. Harayama, "Design of resonant microcavities: application to optical gyroscopes," *Opt. Express* **15**(24), 16245–16254 (2007).
7. J. Li, M.-G. Suh, and K. Vahala, "Microresonator brillouin gyroscope," *Optica* **4**(3), 346–348 (2017).
8. J. Wiersig and M. Hentschel, "Unidirectional light emission from high-Q modes in optical microcavities," *Phys. Rev. A* **73**(3), 031802 (2006).
9. C.-H. Yi, M.-W. Kim, and C.-M. Kim, "Lasing characteristics of a limaçon-shaped microcavity laser," *Appl. Phys. Lett.* **95**(14), 141107 (2009).
10. C. Yan, Q. J. Wang, L. Diehl, M. Hentschel, J. Wiersig, N. Yu, C. Pflügl, F. Capasso, M. A. Belkin, T. Edamura, M. Yamanishi, and H. Kan, "Directional emission and universal far-field behavior from semiconductor lasers with limaçon-shaped microcavity," *Appl. Phys. Lett.* **94**(25), 251101 (2009).
11. J.-W. Ryu and M. Hentschel, "Designing coupled microcavity lasers for high-Q modes with unidirectional light emission," *Opt. Lett.* **36**(7), 1116–1118 (2011).
12. G. D. Chern, H. E. Tureci, A. D. Stone, R. K. Chang, M. Kneissl, and N. M. Johnson, "Unidirectional lasing from InGaN multiple-quantum-well spiral-shaped micropillars," *Appl. Phys. Lett.* **83**(9), 1710–1712 (2003).
13. C.-M. Kim, J. Cho, J. Lee, S. Rim, S. H. Lee, K. R. Oh, and J. H. Kim, "Continuous wave operation of a spiral-shaped microcavity laser," *Appl. Phys. Lett.* **92**(13), 131110 (2008).
14. M. S. Kurdoglyan, S.-Y. Lee, S. Rim, and C.-M. Kim, "Unidirectional lasing from a microcavity with a rounded isosceles triangle shape," *Opt. Lett.* **29**(23), 2758–2760 (2004).
15. I.-G. Lee, S.-M. Go, J.-H. Ryu, C.-H. Yi, S.-B. Kim, K. R. Oh, and C.-M. Kim, "Unidirectional emission from a cardioid-shaped microcavity laser," *Opt. Express* **24**(3), 2253–2258 (2016).
16. J.-W. Lee, C.-H. Yi, I.-G. Lee, J.-H. Kim, H.-H. Yu, K.-R. Oh, and C.-M. Kim, "Extremely high Q and unidirectional laser emission due to combination of the Kolmogorov-Arnold-Moser barrier and the chaotic sea in a dielectric microdisk," *Opt. Lett.* **43**(24), 6097–6100 (2018).
17. J. Ryu, J.-W. Lee, C.-H. Yi, J.-H. Kim, I.-G. Lee, H.-S. Kim, S.-B. Kim, K. R. Oh, and C.-M. Kim, "Chirality of a resonance in the absence of backscatterings," *Opt. Express* **25**(4), 3381–3386 (2017).
18. Y. Kawashima, S. Shinohara, S. Sunada, and T. Harayama, "Self-adjustment of a nonlinear lasing mode to a pumped area in a two-dimensional microcavity," *Photonics Res.* **5**(6), B47–B53 (2017).
19. E. G. Altmann, J. S. E. Portela, and T. Tél, "Leaking chaotic systems," *Rev. Mod. Phys.* **85**(2), 869–918 (2013).
20. E. G. Altmann, "Emission from dielectric cavities in terms of invariant sets of the chaotic ray dynamics," *Phys. Rev. A* **79**(1), 013830 (2009).
21. C.-H. Yi, J.-W. Lee, J. Ryu, J.-H. Kim, H.-H. Yu, S. Gwak, K.-R. Oh, J. Wiersig, and C.-M. Kim, "Robust lasing of modes localized on marginally unstable periodic orbits," *Phys. Rev. A* **101**(5), 053809 (2020).
22. S. H. Oh, C.-W. Lee, J.-M. Lee, K. S. Kim, H. Ko, S. Park, and M.-H. Park, "The design and the fabrication of monolithically integrated GaInAsP MQW laser with butt-coupled waveguide," *IEEE Photonics Technol. Lett.* **15**(10), 1339–1341 (2003).
23. S. H. Oh, J.-U. Shin, Y.-J. Park, S. Park, S.-B. Kim, H.-K. Sung, Y.-S. Beak, and K.-R. Oh, "Fabrication of WDM-PON OLT source using external cavity laser," in *COIN-NGNCON 2006 - The Joint International Conference on Optical Internet and Next Generation Network* (2006), pp. 217–219.
24. M. Hatzakis, B. J. Canavello, and J. M. Shaw, "Single-step optical lift-off process," *IBM J. Res. Dev.* **24**(4), 452–460 (1980).
25. J. Wiersig and J. Main, "Fractal weyl law for chaotic microcavities: Fresnel's laws imply multifractal scattering," *Phys. Rev. E* **77**(3), 036205 (2008).
26. S.-Y. Lee, S. Rim, J.-W. Ryu, T.-Y. Kwon, M. Choi, and C.-M. Kim, "Quasiscattered resonances in a spiral-shaped microcavity," *Phys. Rev. Lett.* **93**(16), 164102 (2004).

27. J. Wiersig and M. Hentschel, "Combining directional light output and ultralow loss in deformed microdisks," *Phys. Rev. Lett.* **100**(3), 033901 (2008).
28. H. G. L. Schwefel, N. B. Rex, H. E. Tureci, R. K. Chang, A. D. Stone, T. Ben-Messaoud, and J. Zyss, "Dramatic shape sensitivity of directional emission patterns from similarly deformed cylindrical polymer lasers," *J. Opt. Soc. Am. B* **21**(5), 923–934 (2004).
29. J. Kullig and J. Wiersig, "Frobenius–perron eigenstates in deformed microdisk cavities: non-hermitian physics and asymmetric backscattering in ray dynamics," *New J. Phys.* **18**(1), 015005 (2016).
30. J.-W. Ryu, S.-Y. Lee, C.-M. Kim, and Y.-J. Park, "Survival probability time distribution in dielectric cavities," *Phys. Rev. E* **73**(3), 036207 (2006).
31. A. I. Rahachou and I. V. Zozoulenko, "Effects of boundary roughness on a Q factor of whispering-gallery-mode lasing microdisk cavities," *J. Appl. Phys.* **94**(12), 7929–7931 (2003).
32. J. Wiersig, "Boundary element method for resonances in dielectric microcavities," *J. Opt. A: Pure Appl. Opt.* **5**(1), 53–60 (2003).
33. M. Hentschel, H. Schomerus, and R. Schubert, "Husimi functions at dielectric interfaces: Inside-outside duality for optical systems and beyond," *Europhys. Lett.* **62**(5), 636–642 (2003).
34. T. Harayama, S. Sunada, and K. S. Ikeda, "Theory of two-dimensional microcavity lasers," *Phys. Rev. A* **72**(1), 013803 (2005).
35. A. Cerjan, Y. Chong, L. Ge, and A. D. Stone, "Steady-state ab initio laser theory for n-level lasers," *Opt. Express* **20**(1), 474–488 (2012).
36. T. R. Chen, L. E. Eng, Y. H. Zhuang, and A. Yariv, "Experimental determination of transparency current density and estimation of the threshold current of semiconductor quantum well lasers," *Appl. Phys. Lett.* **56**(11), 1002–1004 (1990).
37. J. Faist, C. Gmachl, M. Striccoli, C. Sirtori, F. Capasso, D. L. Sivco, and A. Y. Cho, "Quantum cascade disk lasers," *Appl. Phys. Lett.* **69**(17), 2456–2458 (1996).
38. T. Namegaya, N. Matsumoto, N. Yamanaka, N. Iwai, H. Nakayama, and A. Kasukawa, "Effects of well number in 1.3- μm GaInAsP/InP GRIN-SCH strained-layer quantum-well lasers," *IEEE J. Quantum Electron.* **30**(2), 578–584 (1994).
39. P. Aloisi, *Power MOSFET Transistors* (John Wiley & Sons, Ltd, 2010), chap. 1, pp. 1–56.
40. V. S. Pereira and S. Blawid, "Drift-diffusion simulation of leakage currents in unintentionally doped organic semiconductors with non-uniform interfaces," *J. Comput. Electron.* **18**(1), 120–129 (2019).
41. Y. Sun, X. Kang, Y. Zheng, J. Lu, X. Tian, K. Wei, H. Wu, W. Wang, X. Liu, and G. Zhang, "Review of the recent progress on GaN-based vertical power Schottky barrier diodes (SBDs)," *Electronics (Basel, Switz.)* **8**(5), 575 (2019).
42. A. Yariv, *Quantum electronics* (Wiley, 1989).
43. D. Garbuzov, L. Xu, S. R. Forrest, R. Menna, R. Martinelli, and J. C. Connolly, "1.5 μm wavelength, SCH-MQW InGaAsP/InP broadened-waveguide laser diodes with low internal loss and high output power," *Electron. Lett.* **32**(18), 1717–1719 (1996).
44. L. Xu, D. Garbuzov, S. Forrest, R. Menna, R. Martinelli, and J. Connolly, "Very low internal loss, 1.5 μm wavelength SCH-MQW InGaAsP/InP laser diodes with broadened-waveguides," in *Conference Proceedings LEOS'96 9th Annual Meeting IEEE Lasers and Electro-Optics Society*, vol. 1 (1996), pp. 352–353.
45. C.-H. Yi, S. H. Lee, M.-W. Kim, J. Cho, J. Lee, S.-Y. Lee, J. Wiersig, and C.-M. Kim, "Light emission of a scarlike mode with assistance of quasiperiodicity," *Phys. Rev. A* **84**(4), 041803 (2011).
46. J.-W. Lee, C.-H. Yi, M.-W. Kim, J. Ryu, K.-R. Oh, and C.-M. Kim, "Unidirectional emission of high-Q scarred modes in a rounded D-shape microcavity," *Opt. Express* **26**(26), 34864–34871 (2018).